Phenomenological model for the gravitational-wave signal from precessing binary black holes with two-spin effects

Sebastian Khan,[1,2] Katerina Chatziioannou,[3] Mark Hannam,[4] and Frank Ohme[1,2]

[1] *Max Planck Institute for Gravitational Physics (Albert Einstein Institute), Callinstr. 38, 30167 Hannover, Germany*
[2] *Leibniz Universität Hannover, D-30167 Hannover, Germany*
[3] *Canadian Institute for Theoretical Astrophysics, 60 St. George Street, University of Toronto, Toronto, ON M5S 3H8, Canada*
[4] *School of Physics and Astronomy, Cardiff University, The Parade, Cardiff, CF24 3AA, United Kingdom*

(Dated: September 27, 2018)

The properties of compact binaries, such as masses and spins, are imprinted in the gravitational-waves they emit and can be measured using parameterised waveform models. Accurately and efficiently describing the complicated *precessional* dynamics of the various angular momenta of the system in these waveform models is the object of active investigation. One of the key models extensively used in the analysis of LIGO and Virgo data is the *single-precessing-spin* waveform model `IMRPhenomPv2`. In this article we present a new model `IMRPhenomPv3` which includes the effects of two independent spins in the precession dynamics. Whereas `IMRPhenomPv2` utilizes a single-spin frequency-dependent post-Newtonian rotation to describe precession effects, the improved model, `IMRPhenomPv3`, employs a double-spin rotation that is based on recent developments in the description of precessional dynamics. Besides double-spin precession, the improved model benefits from a more accurate description of precessional effects. We validate our new model against a large set of precessing numerical-relativity simulations. We find that `IMRPhenomPv3` has better agreement with the inspiral portion of precessing binary-black-hole simulations and is more robust across a larger region of the parameter space than `IMRPhenomPv2`. As a first application we analyse, for the first time, the gravitational-wave event GW151226 with a waveform model that describes two-spin precession. Within statistical uncertainty our results are consistent with published results. `IMRPhenomPv3` will allow studies of the measurability of individual spins of binary black holes using GWs and can be used as a foundation upon which to build further improvements, such as modeling precession through merger, extending to higher multipoles, and including tidal effects.

PACS numbers: 04.80.Nn, 04.25.dg, 95.85.Sz, 97.80.–d

I. INTRODUCTION

Binary systems of compact bodies such as neutron stars (NSs) and black holes (BHs) generate gravitational waves (GWs) that are detectable by second-generation ground based interferometers. The energy carried away by GWs causes the orbit to decay and the binary to merge on astrophysical time scales. These tiny ripples in spacetime propagate almost completely unaffected through the Universe and have the source properties imprinted in the gravitational waveform. In August 2017 the second observing run (O2) of the detectors aLIGO [1] and Virgo [2] ended, and to date O1 and O2 have resulted in the publication of 6 likely binary black hole (BBH) [3–7] merger events, and the joint GW-electromagnetic observation of a pair of merging NSs [8, 9].

Detection and characterisation of GW signals is carried out by a suite of software pipelines that analyse detector data using a variety of analysis methods [10–14]. Matched-filter-based analyses, used in the search for and parameter estimation [15–17] of GW signals from compact binaries require accurate and computationally-inexpensive models for the GW signals, which are used as *templates*. The need for computationally tractable analyses is best satisfied by frequency-domain models. Moreover, the accuracy of GW signal models and the quantity and quality of the physical effects they include impact both the types of sources GW analyses are sensitive to and the fidelity of the conclusions we draw about their properties.

One such physical effect that has been at the center of waveform-modeling efforts in the recent years is spin-precession: when the binary components' spin angular momenta are misaligned with the orbital angular momentum of the binary, spin-orbit and spin-spin interactions cause the binary orbit to change orientation in space, resulting in modulations in the observed signal amplitude and phase [18, 19]. Modeling these modulations is a challenging task, especially for systems with unequal-mass components that are observed from close to the binary plane, since this case requires accurate modeling of both spin-precession effects and higher modes beyond the dominant $(\ell, |m|) = (2, 2)$ multipoles.

Numerous models have been developed in the recent years with the goal of providing a complete coverage across the BBH parameter space containing all relavent physical effects required for the current sensitivity of GW detectors.

The effective-one-body–numerical-relativity (EOB-NR) model, `SEOBNRv3` [20], built upon the non-precessing model of [21], is a time-domain two-spin precessing model. It provides the $(\ell, |m|) \in ((2, 2), (2, 1))$ multipoles in the co-precessing frame although only the $(2, 2)$ is calibrated to numerical relativity (NR) data. This model has been shown to accurately model the $\ell = 2$ multi-

poles from precessing BBHs [22], however, as it requires the integration of a set of coupled ordinary differential equations it incurs a large computational cost.

The *phenomenological* (phenom) waveform models are typically developed and constructed in the frequency-domain and the precessing model `IMRPhenomP` was presented in [23]. `IMRPhenomP` is built upon the non-precessing model of [24] was later upgraded to `IMRPhenomPv2` which used the non-precessing model of [25, 26]. Despite its computational efficiency `IMRPhenomP` is limited to single-spin effects, though this choice was shown to not lead to appreciable biases in the characterization of the first BBH signal [27, 28]. A time-domain phenom model for precessing BBHs was presented in [29], however, it is restricted to equal-mass BBHs with spin magnitudes up to 0.6.

Recently work has been done to develop models for multipoles beyond the dominant $(\ell, |m|) = (2, 2)$ multipole. The first of such models were the non-spinning EOB-NR model of [30] and a non-spinning phenom model was presented in [31]. The first extension of these higher multipole modes into spinning non-precessing BBHs has been acomplished both by the phenom [32] and Effective-One-Body (EOB) [33] approaches.

An alternative approach to waveform modeling has been successful in building *surrogate* models [34] that interpolate GW data from NR simulations. The surrogate model of [35] is a fully precessing, time-domain model containing $\ell \leqslant 4$ multipoles, however, it is restricted to systems where the ratio of the components' masses is less than two.

In this paper we take another step towards a computationally-tractable GW model that accurately models generic BBH systems by introducing the frequency-domain fully-precessing phenomenological model, `IMRPhenomPv3`, that describes the inspiral, merger, and ringdown phases of spinning BBHs. Our upgrade from `IMRPhenomPv2` to `IMRPhenomPv3` hinges on a novel closed-form solution to the differential equations that describe precession including the effects of radiation reaction in the Post Newtonian (PN) regime where the binary components are well-separated [36, 37]. This closed-form solution to the precession equations including the effects of radiation reaction has been shown to accurately describe precession for systems with generic masses and spins [36]. Moreover, since it is an analytic frequency-domain model, it is also amenable to the reduced-order-quadrature method to greatly accelerate likelihood evaluations for fast parameter estimation [38]. In addition, `IMRPhenomPv2` exhibits non-physical precession behaviour for some high mass-ratio, anti-aligned spin configurations, as discussed in Sec. II D, but this behaviour is not observed in in `IMRPhenomPv3`.

We validate our new model by comparing against a large set of precessing NR waveforms. We find that the improved treatment of the inspiral improves the accuracy of the model for measurement of low-mass systems in LIGO-Virgo data. Finally, as a first application and demonstration of our model's readiness we perform a Bayesian parameter estimation analysis (using `LALInference` [16]) on the GW event GW151226 [4]. This is a $\sim 22\,M_\odot$ BBH signal where at least one of the BHs is measured to have a dimensionless spin magnitude of $\gtrsim 0.2$ at the 99% credible level. The presence of spin and the low total mass, which implies a large number of GW cycles ($\sim$55) measurable by the detector, makes this an ideal candidate to look for evidence of precession. This is the first analysis of GW151226 with a Inspiral-Merger-Ringdown (IMR) precession model with the full 4 degrees of freedom coming from precession.

II. BUILDING THE NEW MODEL

In this section we describe the construction of `IMRPhenomPv3` and highlight the improvements compared to `IMRPhenomPv2`.

A. Precessing BBH phenomenology

A quasicircular BBH system can be parameterised by only 7 intrinsic parameters; the mass-ratio $q = m_1/m_2$[1] and 6 spin angular momenta $\vec{S}_1$ and $\vec{S}_2$. In addition, the total mass $M = m_1 + m_2$ can be factored out and systems with different total masses can be obtained with appropriate scaling of M. For each BBH we can define a Newtonian orbital angular momentum $\vec{L}$, which is perpendicular to the instantaneous orbital plane and a total angular momentum $\vec{J} = \vec{L} + \vec{S}_1 + \vec{S}_2$.

We classify BBH systems into different categories according to their spin. *Non-precessing* systems have BH spins that are either aligned- or anti-aligned with $\vec{L}$. Systems with spins (anti-)aligned with $\vec{L}$ plunge and merge at (larger) smaller separations compared to non-spinning binaries, shifting the merger and ringdown part of the signal to (lower) higher GW frequencies. *Precessing* BBH are systems with arbitrary BH spin orientation. Interactions between the BH spins and $\vec{L}$ introduce a torque on the orbital angular momentum causing it to precess around the (almost constant) direction of the total angular momentum. Special sub-categories of precessing systems include *simple-* and *transitional-*precession binaries [18, 19]. Most binaries undergo simple precession, while transitional precession occurs when $\vec{J} = \vec{L} + \vec{S}_1 + \vec{S}_2 \approx 0$ [18].

B. Modeling precessing BBHs

The complicated phenomenology of generically precessing BBHs makes waveform modeling especially chal-

[1] We use the convention $m_1 \geqslant m_2$.

lenging. A significant advance was achieved when it was observed that the GW signal from precessing binaries is simplified when observed in a frame that is adapted to the precessional motion of the binary [39, 40]. In this non-inertial (co-precessing) frame the z-axis approximately tracks the orientation of the orbital plane. When the waveform is transformed into this frame it closely mimics the signal of the equivalent BBH system that has the spin components perpendicular to $\vec{L}$ set to zero [39, 41]. This is a consequence of the approximate decoupling between the components of spin parallel and perpendicular to $\vec{L}$; the former influences the rate of inspiral and the latter drives the precessional motion [18, 39, 42].

This observation led to a method for building models for the gravitational waveform from generic precessing BBHs by first constructing a model for the gravitational waveform produced by the equivalent non-precessing BBHs and then introducing precession through a time (or frequency) dependent rotation of the signal derived from the orbital dynamics [43]. Colloquially this procedure is denoted "twisting-up" a non-precessing model to produce a precessing model [43].

Beginning with an inertial frame that is aligned with the total angular momentum at some reference frequency $\hat{z} = \hat{J}$ we describe the orbital angular momentum by the azimuthal and polar angles (α, β). In order to completely specify the rotation we use the frame that minimises precessional effects and adopt the "minimum rotation condition" [44] which enforces the third Euler angle to obey $\dot{\epsilon}(t) = \dot{\alpha}(t)\cos(\beta(t))$. This angle constitutes a modification to the orbital phase chosen so that the frequency in the inertial frame is the same as the frequency in the co-precessing frame. For a geometric depiction, see Figure 1 in Ref. [36][2].

This procedure was used to produce the first precessing IMR models [20, 21, 23]. The general procedure is as follows. First we express the two GW polarisations h_+ and $h_\times$ as a linear combination of spherical harmonics with spin-weight -2. The coefficients of the basis functions are the GW multipoles $h_{\ell,m}$, see equation (1). This decomposition is performed in a frame that is aligned with the total angular momentum and the direction of propagation is given by the spherical polar coordinates (θ, φ),

$$h(t;\theta,\phi) = h_+ - ih_\times = \sum_{\ell\geqslant 2,m} h_{\ell,m}(t) Y^{-2}_{\ell,m}(\theta,\varphi). \quad (1)$$

From here we wish to express the GW multipoles from precessing BBHs $h^{prec}_{\ell,m}$ in terms of the multipoles from non-precessing BBHs $h^{non-prec}_{\ell,m}$ and the appropriate angles that describe the "twisting-up" from non-precessional to precessional dynamics. This is done by applying the Wigner-D rotation matrices to the GW multipoles from the non-precessing system using the angles $(\alpha, \beta, \epsilon)$ [39, 40, 43, 44]. Here we focus on the $\ell = 2$ multipoles and the case where the non-precessing model only contains the $\ell = |m| = 2$ multipoles. In that case, the waveform is given by

$$h^{prec}_{2,m}(t) = e^{-im\alpha(t)} \sum_{|m'|=2} e^{im'\epsilon(t)}\, d^2_{m',m}(-\beta(t))\, h^{non-prec}_{2,m'}(t)\,. \quad (2)$$

In order to complete the tranformation from a non-precessing IMR model to a precessing IMR model we also need to modify the mapping between the inspiraling progenitor BHs and the final BH, taking into account the effect of precession. We typically assume that changes in the GW flux due to precession can be neglected so that the estimate of the final mass can be taken from fits to NR simulations of non-precessing systems. The final spin, however, is sensitive to precession and therefore needs to be modified from the model used in the underlying non-precessing model.

In the next sections, we review the angles $(\alpha_{\rm v2}, \beta_{\rm v2}, \epsilon_{\rm v2})$ that were used for the `IMRPhenomPv2` model and then we describe the updated $(\alpha_{\rm v3}, \beta_{\rm v3}, \epsilon_{\rm v3})$ that we employ to produce the updated model `IMRPhenomPv3`.

C. Review of `IMRPhenomPv2`

The method described in the previous section to construct a complete IMR model for precessing BBHs was used to create the `IMRPhenomP` model [23]. The original model used the `IMRPhenomC` [24] model to describe the non-precessing system, but was subsequently enhanced to `IMRPhenomPv2`, which uses `IMRPhenomD` [25, 26], a more accurate aligned-spin model valid for larger mass-ratio binaries and BHs with larger spin magnitudes. Moreover `IMRPhenomD` includes some two-spin information during the inspiral. Both of these underlying aligned-spin models provide only the $\ell = |m| = 2$ spherical harmonic multipole.

In both previous versions of `IMRPhenomP` the precession angles $(\alpha_{\rm v2}, \beta_{\rm v2}, \epsilon_{\rm v2})$ were computed by a closed-form frequency-domain expression derived under the assumption of a single-spin system and parameterised by the aligned effective-spin parameter $\chi_{\rm eff}$ and the precession effective-spin parameter χ_p [45] defined as

$$\chi_p := \frac{\max\left(A_1 S_{1\perp}, A_2 S_{2\perp}\right)}{A_1 m_1^2}\,, \quad (3)$$

where $A_1 = 2 + \frac{3m_2}{2m_1}$, $A_2 = 2 + \frac{3m_1}{2m_2}$ and $S_{i\perp}$ are the magnitudes of the spin-angular momenta perpendicular to $\vec{L}$. Additionally, `IMRPhenomP` used a small-angle approximation for the opening angle (β), an assumption that was subsequently relaxed in `IMRPhenomPv2`.

[2] To convert from the notation used in [36] to ours, use the following substitutions $\phi_z \to \alpha$, $\theta_L \to \beta$ and $\zeta \to \epsilon$.

The expressions for $(\alpha_{\rm v2}, \beta_{\rm v2}, \epsilon_{\rm v2})$ were derived under the stationary phase approximation (SPA) [46] and are used to "twist-up" the entire waveform, including through merger and ringdown, where the assumptions of SPA are formally invalid. Nevertheless the extrapolation of the PN expressions into the merger and ringdown have been shown to not impair the model, so long as the mass-ratio and spin are not large, see [23] and Section III.

`IMRPhenomPv2` uses a single-spin approximation that only models the simple-precession case where the direction of J is relatively constant during the inspiral, and the direction of the final BH spin is assumed to be parallel to J. The magnitude of the final spin angular momentum S_f is computed as the sum of parallel and perpendicular angular momentum components with respect to $\vec{L}$. $S_{\substack{non-\\prec}}$ is the angular momentum from the non-precessing system and $S_\perp$ is the angular momentum of the in-plane spin components.

$$S_f \equiv M_f^2 \chi_f = \sqrt{S_\perp^2 + S_{\substack{non-\\prec}}^2}\,. \tag{4}$$

The final dimensionless spin magnitude χ_f, with a free parameter λ is written as [47, 48]

$$\chi_f = \sqrt{\left(S_\perp \frac{\lambda^2}{M_f^2}\right)^2 + \chi_{\substack{non-\\prec}}^2}\,. \tag{5}$$

The choice made for λ in `IMRPhenomPv2` is $\lambda = M_f/M$ implies that the $S_\perp$ angular momentum gets scaled by the initial total mass. We comment that this is a fairly arbitrary choice as we have a model for M_f that we use in the non-precessing part [25]. However, it was found that this simplification still yielded a model with acceptable accuracy. Finally, $S_\perp$ is approximated using the effective precessing parameter χ_p and computing the angular momentum by assuming only the primary BH has in-plane spin components i.e.

$$S_\perp = m_1^2 \chi_p\,. \tag{6}$$

The model `IMRPhenomPv2` has been used in numerous publications to estimate the source parameters of all BBH observations in the LIGO-Virgo O1 and O2 runs, eg. [4–7, 49–52] and has been the basis of a ROQ approximation to the likelihood [38] that has enabled fast parameter estimation of GW sources [53]. The model's low computational cost has also enabled it to form the basis of the model `IMRPhenomPv2_NRTidal` [54] used for the analysis of the long BNS signal GW170817 [55, 56].

D. Issues with `IMRPhenomPv2` precession angles

Despite `IMRPhenomPv2`'s good performance across the parameter space, there are some known issues with the precession angles. Specifically, the angle $\alpha_{\rm v2}(f)$ is written as a power series in f, including terms up to next-to-next-to-leading order (3PN) in the spin. The leading-order Newtonian term (see, for example, Ref. [18]) is

$$\alpha_{\rm v2}^N = \alpha_0 - \frac{20\left(1 + \frac{3}{4q}\right)}{192 f}, \tag{7}$$

where α_0 is a constant. At this order, the precession angle is a monotonically increasing function, which is what we expect in a physical system exhibiting simple precession: the orbital angular momentum vector precesses around the total angular momentum throughout the binary's evolution, and the rate of precession steadily increases. At leading order [18] we also see that the precession angle (and therefore also the precession frequency) depend only on the mass-ratio of the binary; the spin affects the precession rate at higher orders.

If we extend this expression up to $f^{1/3}$, as is done in the NNLO expressions used in `IMRPhenomPv2` [57] (which also include a $\log(f)$ term), then higher order terms can enter with opposing signs. In some cases this can remove the monotonicity of $\alpha_{\rm v2}(f)$, even for simple-precession configurations where we know that such behavior is not physically consistent.

Figure 1 show examples of this behavior. We first consider a configuration that is comparable to those already found in GW observations: the mass ratio is 1, the component of the spin parallel to the orbital angular momentum is zero, i.e., $\chi_{\rm eff} = 0$, and the larger BH has a spin of magnitude 0.9 lying in the orbital plane, i.e., $\chi_p = 0.9$; since χ_p has not been constrained in observations to date, a value of 0.9 is consistent with the measured parameters. The angle of the spin in the plane at a particular reference frequency determines the constant α_0, but we will focus here on the frequency evolution of the precession angle. We plot the precession angle $\alpha_{\rm v2}(f) - \alpha(f_0)$, where $Mf_0 = 0.0001$, which corresponds to approximately 2 Hz for a binary with a total mass of $10\,M_\odot$. The results are shown up to the Schwarzschild ISCO frequency ($Mf = 0.0217$). We can see that $\alpha_{\rm v2}(f)$, as predicted by the leading-order Eq. 7 (blue dashed line), the full NNLO expressions used for `IMRPhenomPv2` (blue solid line), the full `IMRPhenomPv3` expression (orange dashed line), and the trunchated `IMRPhenomPv3` expression (orange solid line) all agree well, even though spin effects are not included in the leading-order result.

In the second example, we can see that the NNLO expression is needed to accurately describe the precession for higher mass ratios and higher spins. This example shows $\alpha_{\rm v2}(f) - \alpha(f_0)$ for a binary with mass-ratio 8, again $\chi_{\rm eff} = 0$ and $\chi_p = 0.9$. The NNLO `IMRPhenomPv2` and the `IMRPhenomPv3` expressions agree well, but the leading-order expression accumulates a difference against the others of ∼60 rad, or ∼10 precession cycles, out of ∼47 cycles over the course of the entire inspiral. This level of agreement between the `IMRPhenomPv2` and `IMRPhenomPv3` expressions is typical

across all configurations with mass ratios up to ∼5, so we can be confident that IMRPhenomPv2 accurately models the precession angle α_{v2} with sufficient accuracy for aLIGO and Virgo BBH observations to date.

In the third example, the mass-ratio is 10, but now $\chi_{\rm eff} = -0.8$, $\chi_p = 0.1$. Now the IMRPhenomPv2 expressions disagree significantly between each other and against the IMRPhenomPv3 expressinos. Most notable, however, is that the IMRPhenomPv2 precession angle (shown alone in the fourth panel of Fig. 1) reaches a maximum and then decreases; the maximum implies that at this point the precession comes to a halt, and then continues in the opposite direction. This occurs at a frequency of $\sim 10\,$Hz for a $10\,M_\odot$ binary, i.e., many orbits before merger, while the system should still be undergoing simple precession, and when PN results should still be valid. Indeed, simple precession does continue through these frequencies in an evolution of the PN equations of motion, as indicated by the $\alpha_{v3}(f)$ results shown in the third panel. We therefore conclude that the NNLO frequency expansion behaves unphysically for certain mass-ratio and spin combinations, and will degrade the accuracy of a model in these regions of parameter space.

E. Upgrading to IMRPhenomPv3

The first closed-form analytic inspiral waveform model for generically precessing BBHs was presented in [36, 37]. The solution utilized two ingredients. First, the analytic solution to the conservative precession equations constructed in [58] was supplemented by radiation-reaction effects through a perturbative expansion in the ratio of the precession to the radiation reaction time scale [59, 60] known as multiple scale analysis (MSA) [61]. Second, the frequency-domain waveform was analytically computed through the method of shifted uniform asymptotics (SUA), first introduced in [62]. The resulting inspiral waveform model for the precession dynamics incorporates spin-orbit and spin-spin effects to leading order in the conservative dynamics and up to 3.5PN order in the dissipative dynamics ignoring spin-spin terms.

We use the generic two-spin solution of [36, 37] to obtain two-spin expressions for the precession angles $(\alpha_{v3}, \beta_{v3}, \epsilon_{v3})$. Specifically we use Eqs. (58), (66), (67) and the coefficients in Appendix D in [36] for α_{v3} (denoted as ϕ_z in that paper). Appendix F in [36] provides the analogous equations and coefficients for the ϵ_{v3} angle (called ζ in [36]), while the β_{v3} angle (called θ_L in [36]) is given by Equation (8).

As an illustration of the new waveform model we compare IMRPhenomPv2 (blue-dashed) and IMRPhenomPv3 (orange-solid) for a mass-ratio 1:10, two-spin system in Figure 2. The top left panel shows the $h_\times(t)$[3] GW polarisation viewed at an inclination angle[4] of 90 deg. The top right panel is a zoom in around the merger. At early times both models are in agreement however, due to the difference between the precession angle models the two models start to noticeably disagree around 90 s before merger.

Similarly to the angles α_{v2} and ϵ_{v2}, the expressions for α_{v3} and ϵ_{v3} involve series expansions in terms of the GW frequency. The expression for ϵ_{v3} is fully expanded and expressed in terms of a power series of the GW frequency, $f^{-4/3+n/3}$, $n \in [1, 6]$. The angle α_{v3} involves both expanded ($n \in [1, 6]$) and un-expanded terms, a choice made to increase the angle's accuracy for unequal-mass systems, as discussed in Sec. IV D 1 of [36]. The order to which we truncate the relevant expansions can impact the accuracy of the model: too few n terms and the expansion fails to accurately describe the inspiral but too many n terms and the expressions become inaccurate when extrapolating towards higher frequencies. Figure 2 illustrates the impact of expansion order n on the precession angles. The lower-left and lower-middle panels show the α_{v3} and ϵ_{v3} angles as a function of the GW frequency. The solid-orange line shows the model that is used in IMRPhenomPv3 and the paler curves show different the result for truncation orders for the α_{v3} and ϵ_{v3} models. The dashed-blue line shows the results for the precession angle model used in IMRPhenomPv2 which deviates away from the other approximations. The α_{v2} angle in particular shows qualitatively different behaviour, growing rapidly as the frequency increases.

We also have a choice when computing β_{v3}, the angle between $\vec{J}$ and $\vec{L}$. We investigated either using Newtonian order, 2PN Non-Spinning (as was done in IMRPhenomPv2) and also a 3PN version including spin-orbit terms for the magnitude of $\vec{L}$ that is used in the computation of β_{v3}. A comparison between the different methods for calculating β_{v3} can be seen in the lower-right panel in Fig. 2. The observed modulations are nutation due to spin-spin effects.

The three vertical black lines (from left to right) are the hybrid-MECO [63], Schwarzschild ISCO and the ringdown frequency for this system. We assume the limit to which PN results can be reliably used to be near the hybrid-MECO/Schwarzschild ISCO and the region between this and the ringdown frequency to be the region where we are extrapolating the precession angles beyond their assumed region of validity. This assumption appears to hold as it seems to track the location of a turnover point in many of the precession angle variants, a feature that is unphysical (at least in simple precession cases) as discussed in Sec. II D.

To decide which choices when computing the precession anlges lead to the most accurate model we performed several mismatch calculation comparing different

[3] The time domain $h_\times(t)$ was obtained by computing the inverse Fourier transform of $\tilde{h}_\times(f)$.

[4] Inclination is the angle between the $\vec{L}$ and the line of sight.

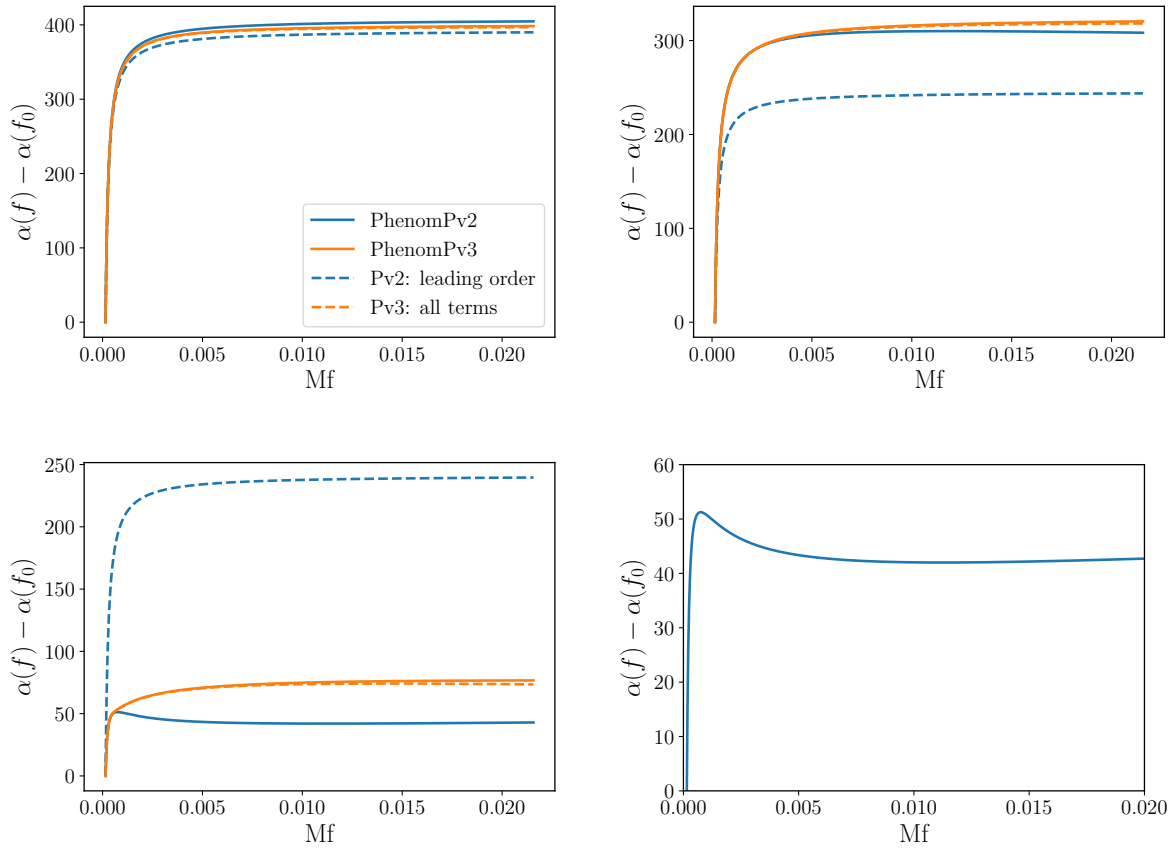

FIG. 1. Comparison of leading-order (`IMRPhenomPv2: leading order`), NNLO (`IMRPhenomPv2`), full-PN (`IMRPhenomPv3: all terms`), and the version we adopt in the final model (`IMRPhenomPv3`) expressions for the precession angle, α. First panel: $q = 1$, $M_{\rm tot} = 10M_\odot$ $\chi_{\rm eff} = 0$, $\chi_p = 0.9$; second panel: $q = 8$, $M_{\rm tot} = 10M_\odot$ $\chi_{\rm eff} = 0$, $\chi_p = 0.9$; third panel: $q = 10$, $M_{\rm tot} = 10M_\odot$ $\chi_{\rm eff} = -0.8$, $\chi_p = 0.1$; fourth panel: same configuration as third panel, but zoom of non-physical behavior of $\alpha_{\rm v2}(f)$. All cases are generated from a frequency of 2 Hz. See text for discussion.

versions of the model with NR. We find that most choices lead to reasonably accurate models for the inspiral but, however, can lead to suboptimal performance during the merger. We obtain an accurate model for the entire coalescence by using all but the highest order terms in the expressions for $\alpha_{\rm v3}$ and $\epsilon_{\rm v3}$ and to use the highest order PN calculation available namely, with 3PN with spin-orbit terms when computing $|\vec{L}|$ in the β angle. In Sec. III we only show results for the final model.

To minimise differences bewteen `IMRPhenomPv2` and `IMRPhenomPv3` we adopt the same model for the final spin however, we note a simple extension would be to include all in-plane spin components in the calculation of $S_\perp$ and relaxing the approximation that $M_f = M_i$ by using the final mass model used in the non-precessing case. This will be done in following work.

We also note one other improvement on `IMRPhenomPv2`, which deals with "superkick" configurations [64]. These are equal-mass configurations where each black hole has the same spin, but the spins both lie in the orbital plane and point in opposite directions. These configurations possess symmetry such that the orbital plane does not precess, but instead "bobs" up and down as linear momentum is radiated perpendicular to the orbital plane. If `IMRPhenomPv2` is given the parameters for such a configuration, the definition of χ_p, Eq. (3) will yield a non-zero value, and the code will construct the waveform for a precessing system. Neighbouring configurations in parameter space will display similar behaviour, and `IMRPhenomPv2` will again generate the "wrong" waveform. By correctly accounting for both spins, `IMRPhenomPv3` corrects this problem. A request for an equal-mass superkick configuration will yield the waveform for an equal-mass nonspinning configuration, which is the closest approximation that does not experience recoil.

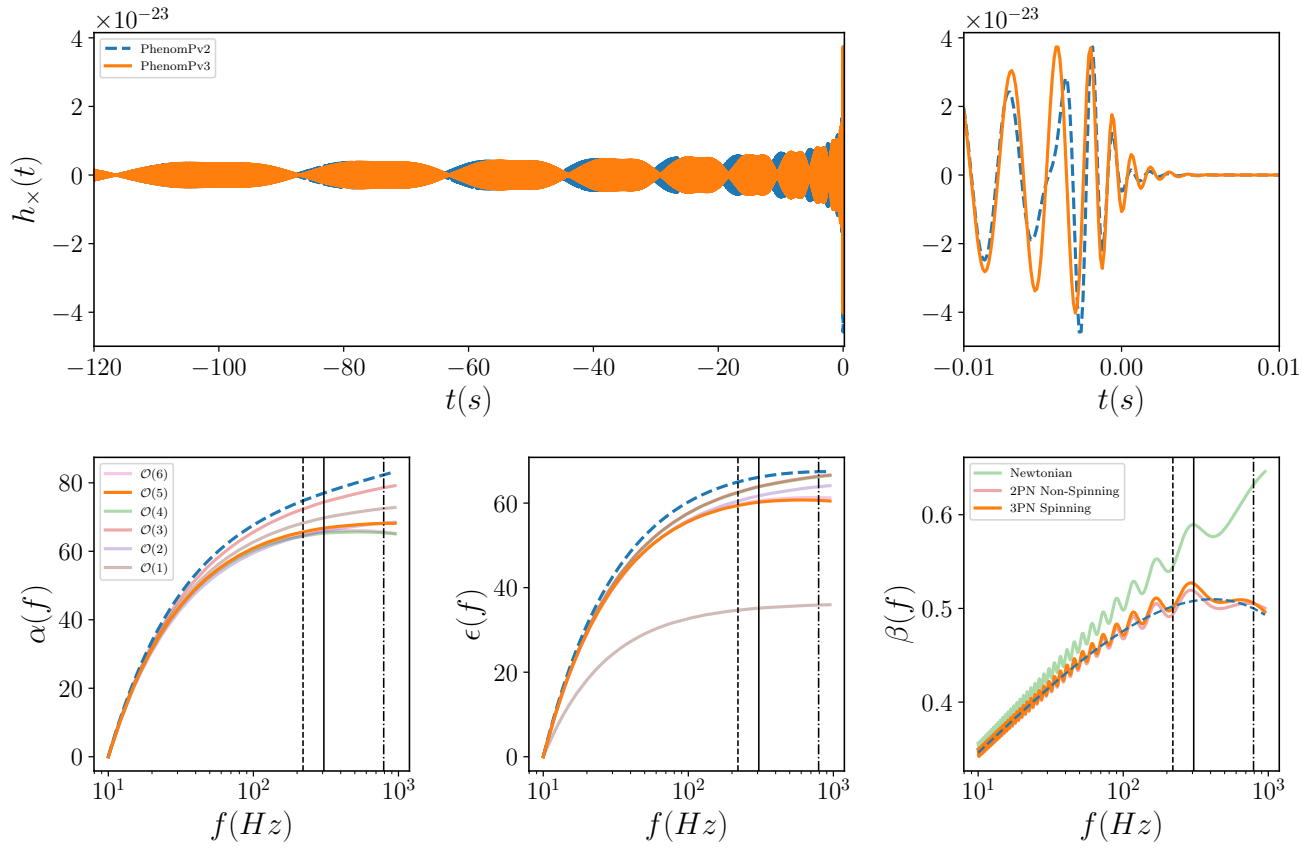

FIG. 2. Composite figure comparing the various models for the precession angles and their overall effect on the waveform. We generate the gravitational waveform from a BBH system with the following parameter: $q = 10$, $M = 20$, $S_1 = (0.4, 0, 0.4)$, $S_2 = (0.3, 0, -0.3)$, $f_{\rm start} = 10$Hz. The top row shows $h_\times$ polarisation evaluated at $\iota = \pi/2$ (Here ι is the angle between $\vec{L}$ and the line of sight). In all panels the dashed blue line corresponds to `IMRPhenomPv2` and the solid orange line corresponds to `IMRPhenomPv3`. Top left: The full waveform generated from 10Hz. Top right: Zoom in around merger. The early-time agreement and late-time disagreement demonstrates the agreement between the two models of precession at low frequencies and disagreement at high frequencies. Bottom row shows the precession angles as a function of GW frequency. Bottom left: α. Bottom middle: ϵ. Bottom right: β. The solid black line is the hybrid-MECO frequency [63], the dashed black line is the Schwarzschild ISCO frequency and the dot-dashed black line is the ringdown frequency for this system. The legend in the bottom left plot applies to the bottom middle plot as well and shows to what n order (see text) the α and ϵ angles where expanded. The legend in the bottom right figure indicates if aligned-spins were included in the calculation of the magnitude of the orbital angular momentum.

III. COMPARISON TO NUMERICAL RELATIVITY

In this section we compare `IMRPhenomPv3` to a large number of NR simulations of precessing BBHs and show the excellent agreement between our model and the simulations.

A. Mismatch calculation

In GW searches and parameter estimation, template waveforms are correlated with detector data. This operation can be written as an inner-product weighted by the sensitivity of the detector (described by the power spectral density (PSD) $S_n(f)$) between the real valued template $h(t)$ and signal $s(t)$ waveforms. We define the *overlap* between the template and signal as

$$\mathcal{O} \equiv (h|s) \equiv 4\,\mathrm{Re}\int_{f_{\rm min}}^{f_{\rm max}} \frac{\tilde{h}^*(f)\tilde{s}(f)}{S_n(f)} df\,, \tag{8}$$

where $\tilde{h}$ representes the Fourier transform of h and $\tilde{h}^*$ is the complex conjugate of $\tilde{h}$.

This inner-product is closely related to the definition of the matched-filter signal-to-noise ratio (SNR) and indeed the $1-\mathcal{O}$ between normalised waveforms ($\hat{x} = \sqrt{(x|x)}$) is

directly proportional to the loss in SNR making it a useful metric to measure the accuracy of waveform models.

Aside from the masses and spins of the BHs the GW signal depends on a number of extrinsic parameters: the direction of propagation in the source frame (ι, ϕ_0), a polarisation angle ψ, a reference time t_0 and the luminosity distance D_L. The dependency of the observed GW signal on the polarisation angle (ignoring the angular position of the source with respect to a detector) is given by

$$h(t) = h_+(t)\cos(2\psi) + h_\times(t)\sin(2\psi)\,. \tag{9}$$

Given two waveforms h and s we quantify the agreement between them by computing their normalised overlap subject to various averages and optimisations of extrinsic parameters whilst keeping the intrinsic parameters fixed. Note that the use of normalised waveforms $\hat{h}$ and $\hat{s}$ factors away the dependency of the D_L in the overlap.

In particular for each inclination angle ι considered we compute the overlap between $\hat{h}$ and $\hat{s}$ with the same masses and spins and vary the extrinsic *signal* parameters (ϕ_0^s, ψ_0^s) by evaluating them on a 10×10 grid with the following domain $\phi_0^s \in [0, 2\pi]$ and $\psi_0^s \in [0, \pi/4]$. For each point on this grid we analytically maximise over a time shift using an inverse Fourier transform, analytically maximise over ψ_0^h according to the method detailed in [65] and finally numerically optimise over ϕ_0^h using optimisation routines from the `SciPy` package [5]. From here we define the *match* as a function of the extrinsic parameters of the signal as

$$\mathcal{M}(\phi_0^s, \psi_0^s) \equiv \max_{t_0^h, \phi_0^h, \psi_0^h} (\hat{h}|\hat{s}(\phi_0^s, \psi_0^s))\,. \tag{10}$$

Next we average over the extrinsic parameters of the signal (ϕ_0^s, ψ_0^s) weighted by its optimal SNR ρ at each point which accounts for the likelihood that this signal would be detected [42, 66]. We call this the *orientation-averaged-match*

$$\overline{\mathcal{M}} \equiv \left(\frac{\sum_i \rho_i^3 \mathcal{M}_i^3}{\sum_i \rho_i^3} \right)^{1/3}\,. \tag{11}$$

From here we define the *orientation-averaged-mismatch* as $1 - \overline{\mathcal{M}}$. We will quote results in terms of this. In what follows we shall use h to denote a *template* waveform, i.e., generated by a waveform approximant and s to denote the *signal* waveform which will be an NR waveform.

We compute the orientation-averaged-mismatch between the template waveform and each NR waveform at three different inclination angles $(0, \pi/3, \pi/2)$ rad. By increasing the inclination angle we tend to observe a weaker but more modulated waveform due to the precession. We therefore expect the accuracy of the models to decrease at inclined orientations where the effects of precession are typically more prounounced. We consider 3 different waveform approximants: `IMRPhenomPv2`, our improvement `IMRPhenomPv3` and the precessing IMR EOB-NR model `SEOBNRv3` [22]. For each NR simulation we generate a template with the same masses and spins beginning from the start frequency as reported in the NR metadata. Waveforms were generated using the `LALSimulation` package, part of the software library `LALSuite` [67], using the NR injection infrastructure presented in [68].

When comparing GW signal models with NR there is an ambiguity that one encounters when trying to identify a time (or frequency) in the gravitational waveform and the corresponding retarded time (or frequency) of the BBH dynamics, where spins are measured and defined in the NR simulation [69]. This complicates the comparison of precessing systems because the orientation of the spin is now time dependent.

To account for the ambiguity in how the spins are defined we allow the frequency at which the spins are specified to vary. This is similar to what was done in Ref. [22] where `SEOBNRv3` was compared to a similar set of NR waveforms. In `IMRPhenomPv2` and `IMRPhenomPv3` we can fix the start frequency, $f_{\rm start}$, and vary the spin-reference-frequency ($f_{\rm ref}$), however, in the `LALSuite` implementation of `SEOBNRv3` this is not possible and instead the spins are defined at the start frequency. Therefore we perform the optimisation of spin-reference-frequency slightly differently between the two phenom models and the EOB-NR model. We numerically optimise using `SciPy` for both cases. For the phenom models we allow $f_{\rm ref}$ to vary in the following range $[0.8, 1.4] \times f_{\rm start}$ and for `SEOBNRv3` we vary $f_{\rm start}$ in the same range but if $1.4 f_{\rm start}$ is greater than the maximum start frequency allowed by the EOB-NR generator, $f_{\rm max}^{\rm EOB}$, then we use this[6]. For long waveforms the variation in the resulting match is less that 1% however, for shorter waveforms, such as SXS:BBH:0165, the variation can be as larger as 8%.

Our NR signal waveforms only contain the $\ell = 2$ multipoles which is a good approximation for comparable mass systems $q \lesssim 3$ and for small inclinations where the effect of precession on the waveform is minimised. This assumption breaks down for some of the cases we consider here but we are primarily concerned with how faithful our new model is to a signal which contains the modes that we have modelled. We also want to keep separate systematic errors due to neglecting $\ell > 2$ modes and those due to inaccuracies in modelling the $\ell = 2$ modes. We

[5] Because we are comparing generic precessing waveforms we can not analytically optimise over ϕ_0^h in the presence of $m \neq 2$ multipoles.

[6] $f_{\rm max}^{\rm EOB}$ is equal to the the orbital frequency at a separation of $10M$.

compute the match assuming the theoretical design sensitivity of one of the LIGO detectors (zero de-tuned high power PSD [70]) and starting from a low frequency cutoff of 10 Hz until the end of the waveform. We compute the match over a range of total masses spanning from $20\,M_\odot$ to $200\,M_\odot$. If the NR waveform is not long enough to start at 10 Hz then we use the starting frequency of the NR waveform as the low frequency cutoff in the match integral.

B. NR catalogue

We use the SXS public catalogue [71, 72] of NR waveforms as our validation set consisting of 90 precessing waveforms with mass-ratios between 1:1 and 1:6. Figure 3 presents an illustration of the parameter space covered. This set of NR waveforms mainly covers the mass-ratio space between 1:1 and 1:3 with only 3 waveforms above this: 2 at mass-ratio 1:5 and one at 1:6. This is clearly a heavily undersampled region of parameter space across NR groups (see other public catalogues from RIT [73, 74] and GaTech [75, 76]). The vast majority of cases also have spin magnitudes that are $\leqslant 0.5$ however there is one case (SXS:BBH:0165) where $|\vec{\chi}| = 0.9$. However, this is a short waveform of only 6 orbits in length. Again this highlights the need for longer NR simulations of BBHs with $|\vec{\chi}| > 0.5$ across all mass-ratios.

The bottom panel of Fig. 3 illustrates the length of the NR simulations. It shows the start frequency, in Hz, of the $\ell = |m| = 2$ GW multipole when the BBH system is scaled to $50M_\odot$. In order for a NR waveform to be used in the analysis of LIGO-Virgo data, without hybridising to PN, the waveform needs to span the sensitive region of the detector, a typical start frequency for current instruments is between $20 - 25$Hz (see Figure 2 of [6]). We see that for a BBH of total mass $50M_\odot$, similar to GW150914 [3], that many of these cases start at around 20Hz. Again there are a couple of outliers at mass-ratios 1:5 and 1:6.

C. Results

Figure 4 shows the results of the orientation-averaged-mismatch $(1 - \overline{\mathcal{M}})$ calculation as a function of the total mass. Each row corresponds to a fixed template waveform labeled in the top left of each plot in the first column. From top to bottom each row show results for `IMRPhenomPv2`, `IMRPhenomPv3` and `SEOBNRv3`. From left to right each column corresponds to the three different inclination angles we tested $0, \pi/3$ and $\pi/2$ respectively.

First we note that, for all three models, the majority of cases have mismatches smaller that 3% and many smaller than 1%. This is in agreement with the findings of Ref [22]. Interestingly we find that the mismatch varies weakly with inclination angle indicating that the models perform well even when precession effects are amplified. One of the key results is the superior performance of `IMRPhenomPv3` for total masses between $20 - 50M_\odot$ where all but one case (SXS:BBH:0165 is discussed below) have mismatches $\lesssim 1\%$. We attribute this to the more accurate and reliable new model of the precession dynamics of [36, 37].

To highlight regions of parameter space where current models are least accurate we have compiled Table I, which lists the SXS catalogue number, their mass-ratio and initial spin components if at *any* point the mismatch is greater than 3%. In the table we report the orientation-averaged-mismatch averaged over all total masses for each inclination angle. We also colour these cases in Figure 4.

Our expectation that higher mass-ratio systems will yield the least accurate results due to the fact that precession is based on a PN model and not calibrated to NR, is borne out in our results. Out of all the worst cases, with the exception of SXS:BBH:0161, the worst cases have mass-ratios $\geqslant 3$. SXS:BBH:0161 is the only equal-mass outlier with worst mismatch marginally greater than 3 % for `IMRPhenomPv2`. For `IMRPhenomPv3` and `SEOBNRv3` the accuracy is better than 1 % for all the vast majority of cases.

The case with the highest mismatch, across all templates, is SXS:BBH:0165. This is a mass-ratio 1:6 system with initial spins $S_1 = (0.74, 0.19, -0.50)$ and $S_2 = (-0.19, 0, -0.23)$ with a length of $\sim$ 6.5 orbits. `IMRPhenomPv2` has a best mismatch of $\sim$ 12%. `IMRPhenomPv3` substantionally improves upon this with a worst mismatch of $\sim$ 3.6%. `SEOBNRv3` performs well achieving a worst mismatch of $\sim$ 1.3%. Given that the precession, in all three IMR models, is modelled with uncalibrated PN or EOB calculations, it is not surprising that the region of parameter space where the models do worst comes from high mass-ratios and high spin magnitudes. This is, by far, the case with the most dramatic improvement. In terms of its place in parameter space it has the largest mass-ratio and spin magnitude.

Out of the two mass-ratio 1:5 systems one of them has a worst mismatch larger than 3%. This case, SXS:BBH:0058, is also the longest mass-ratio 1:5 case with approximately 28 orbits. We improve from a worst mismatch of 3.3% with `IMRPhenomPv2` to 2.2% with `IMRPhenomPv3`. `SEOBNRv3` shows good agreement with a worst average mismatch of $\sim 1.4\,\%$.

For cases with mass-ratio 1:3 we find that only 1 (SXS:BBH:0049) out of the 15 cases has a mismatch larger than 3%. The mismatch is worst for `IMRPhenomPv2` and only goes marginally above 3 % for the $\iota = \pi/2$ case where we expect the effects of precession to be most pronouced. With `IMRPhenomPv3` we improve, across all inclinations, with average mismatches between $1 - 2\,\%$. We find a similar performance with `SEOBNRv3`.

Note however, that all the mass-ratio 1:3 and 1:5 systems all have spin magnitudes $\leqslant 0.5$. Validating precessing waveform models at large spin magnitudes requires more NR simulations to be performed. We high-

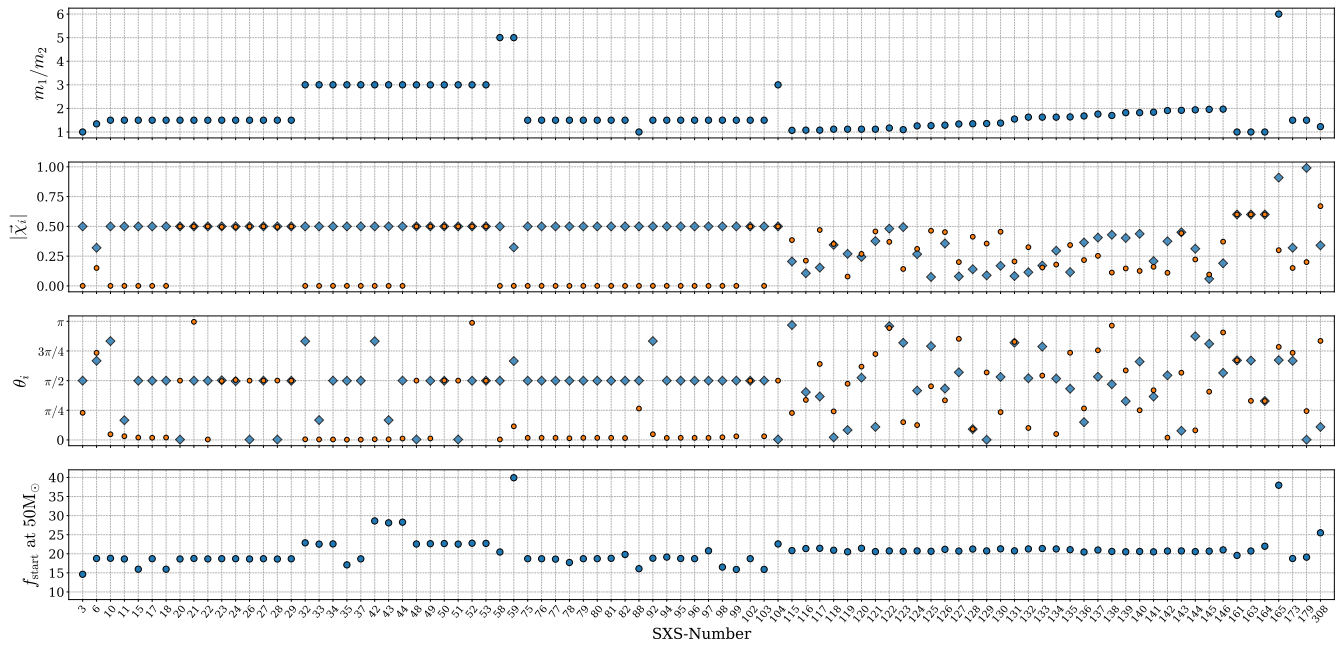

FIG. 3. The precessing parameter space we probe using the SXS public catalogue. The x-axis is the SXS catalogue number. The four panels (from top to bottom) show the mass-ratio $q = m_1/m_2$, the dimensionless spin magnitudes $|\vec{\chi}_i|$, the polar angle between the Newtonian orbital angular momentum and the individual BH spin vectors θ_i where $i = 1, 2$ for the larger and smaller BH respectively and finally the last panel plots the start GW frequency for each simulation when scaled to a total mass of $50{\rm M}_\odot$. Where the primary and secondary BHs are plotted as blue diamonds and orange circles respectively.

Waveform Model	`IMRPhenomPv2`			`IMRPhenomPv3`			`SEOBNRv3`		
SXS:BBH:ID	0	$\pi/3$	$\pi/2$	0	$\pi/3$	$\pi/2$	0	$\pi/3$	$\pi/2$
0049 [$q=3$, $\vec{S}_1=(0.5,0,0)$, $\vec{S}_2=(0,0,0.5)$]	0.7	1.5	2.4	0.9	1.4	1.8	1.0	1.5	1.8
0058 [$q=5$, $\vec{S}_1=(0.5,0,0)$, $\vec{S}_2=(0,0,0)$]	1.2	2.0	3.3	1.3	1.2	2.2	0.2	0.5	1.4
0161 [$q=1$, $\vec{S}_1=(0.52,0,-0.3)$, $\vec{S}_2=(0.52,0,-0.3)$]	1.0	1.1	1.4	0.2	0.6	0.7	0.8	0.6	0.7
0165 [$q=6$, $\vec{S}_1=(0.74,0.19,-0.50)$, $\vec{S}_2=(-0.19,0,-0.23)$]	15.4	12.5	12.1	3.6	3.5	3.0	1.2	1.1	1.3

TABLE I. Percentage mismatches averaged over all total masses for each the three inclination angles (rad) considered. All cases that have a mismatch larger than 3% are shown. The first column shows the SXS ID number with the mass-ratio and initial spin vectors in parentheses.

light again that these comparisons only include the $\ell = 2$ multipoles in the signal waveform and for larger mass-ratio systems ($q \gtrsim 3$) negleting the higher multipoles is no longer a good approximation to the full GW signal.

IV. GW151226 ANALYSIS

As a first application of the new `IMRPhenomPv3` model we study whether the improved two-spin prescription allows for improved parameter extraction from existing GW signals. We focus on event GW151226 as it is the only system with strong support for at least one spinning BH [4, 53]. In spite of this, GW151226 has never been analyzed with a precessing model that employs two-spin dynamics: on the one hand, GW151226 has a low-enough total mass that an analysis with `SEOBNRv3` is not computationally feasible; simultaneously, GW151226 is so massive that the merger phase of the coalescence is in band, making an analysis with precessing inspiral-only models, such as `SpinTaylorT4`, incomplete.

The new `IMRPhenomPv3` waveform model constructed here meets both criteria of computational efficiency and full coalescence description, allowing us to perform the first two-spin analysis of GW151226. We use the Bayesian Inference code `LALInferenceNest` [77] and publicly available data from the LIGO Open Science Centre (LOSC, `losc.ligo.org`). We estimate the power spectral density noise using on-source data and the `BayesWave` algorithm [78, 79]. We marginalise over detector calibration amplitude and phase uncertainty using values provided in [52]. We use a spin prior that is

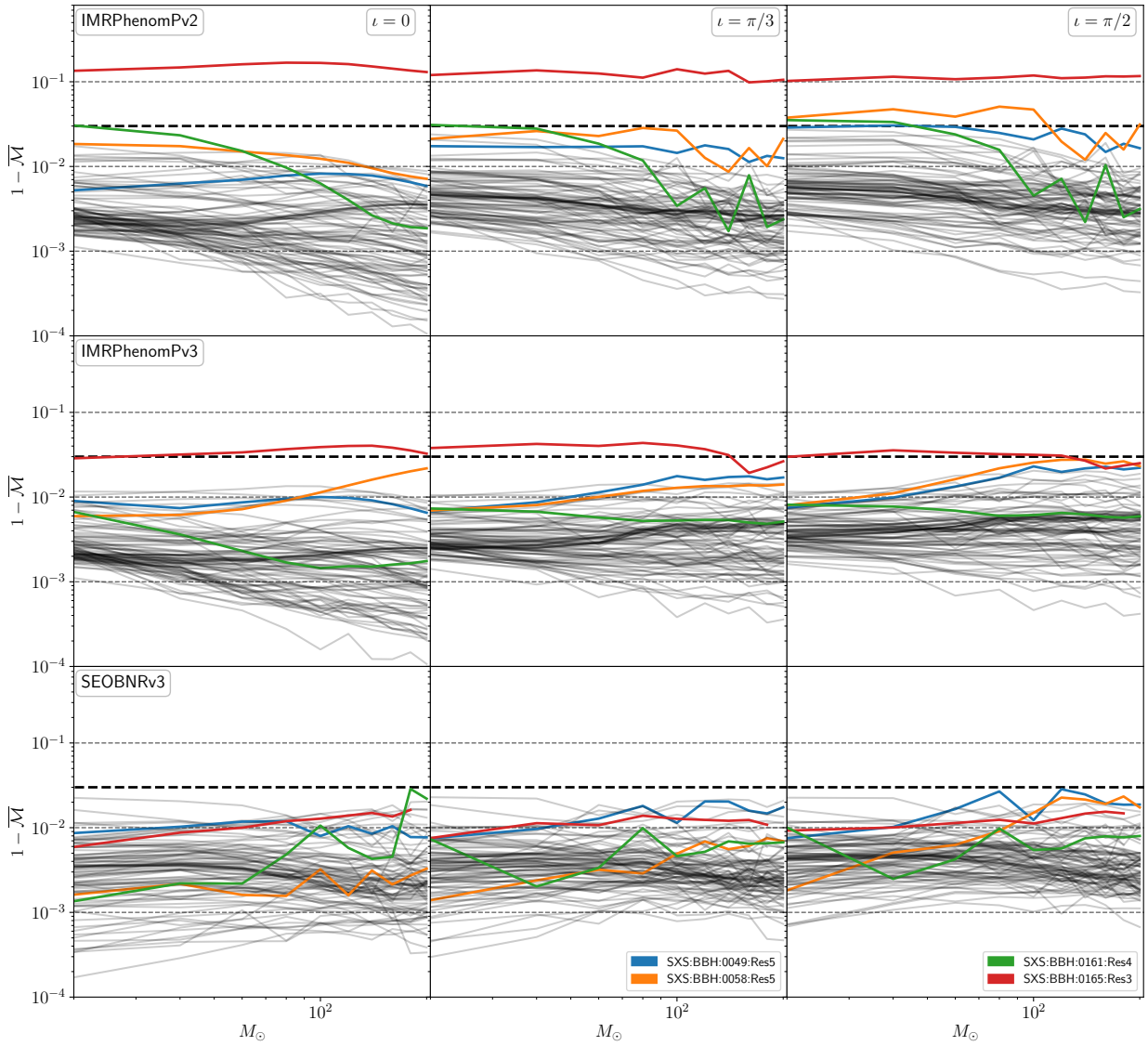

FIG. 4. The results of the comparison between `IMRPhenomPv2` (first row), `IMRPhenomPv3` (second row) and `SEOBNRv3` (third row) and the precessing NR simulations from the public SXS catalogue. Each column shows the results for $\iota = (0, \pi/3, \pi/2)$, from left to right. Where ι is the angle between the Newtonian orbital angular momentum $\vec{L}$ and the line-of-sight, at the start frequency. The figure shows the orientation-averaged-mismatch $(1 - \overline{\mathcal{M}})$ as a function of the total mass (log scale). Cases which have a maximum mismatch greater than 3% are coloured and presented in Table I.

uniform in direction and magnitude up to 0.89. In what follows, we present and compare results obtained using `IMRPhenomPv2` using a reduced-order-quadrature approximation to the likelihood [38] and `IMRPhenomPv3`.

Table II presents our results for the intrinsic parameters. We quote the median value from the 1-D marginalised posterior and the associated 90% symmetric credible interval. Noteworthy differences are a broader uncertainty in the primary mass resulting in `IMRPhenomPv3` favouring a slightly more asymmetric system, although both models are within the statistical uncertainty of each other. Overall we find consistent results between the two models as well as the published LIGO-Virgo Collaboration (LVC) analysis [52]. We also have an estimate of the Bayes factor for a coherent signal across the two LIGO detectors versus an incoherent signal or noise. We find a slightly larger Bayes factor for `IMRPhenomPv3` despite the extra degrees of freedom from

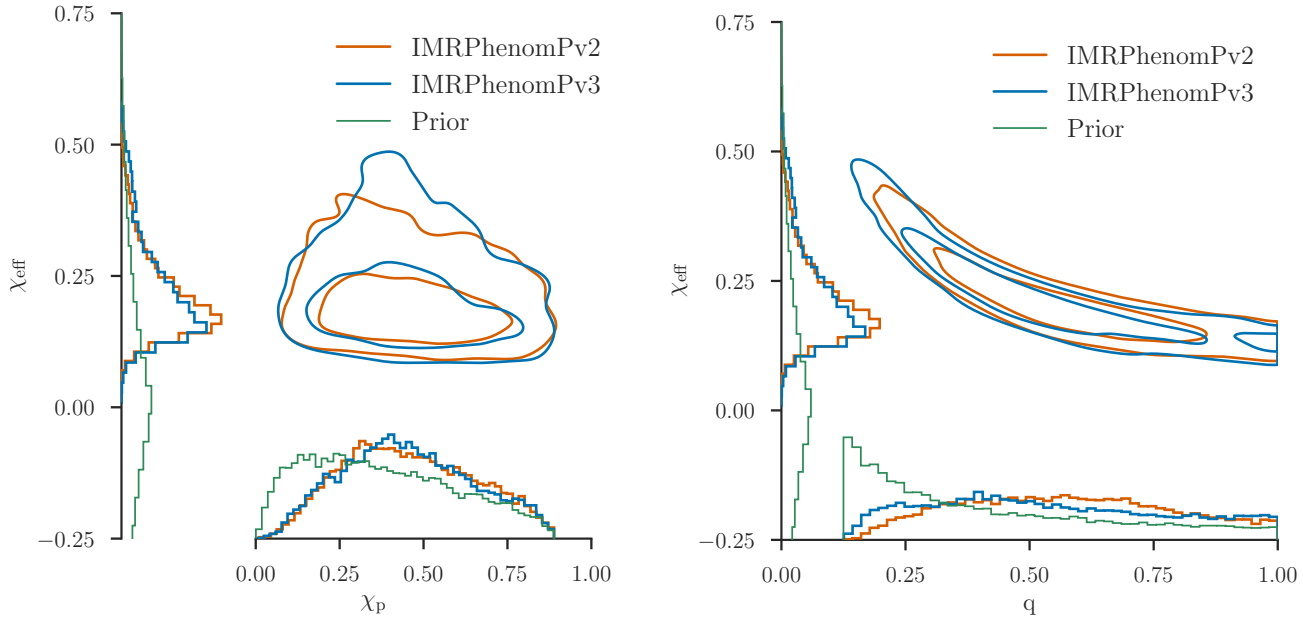

FIG. 5. Posterior probability densities for $\chi_{\rm eff} - \chi_p$ (left) and $\chi_{\rm eff} - q$ (right) for GW151226 using `IMRPhenomPv2` and `IMRPhenomPv3`. Despite the more accurate description of 2-spin dynamics of `IMRPhenomPv3` the posteriors are consistent, demonstrating the difficulty of measuring 2-spin dynamics.

the full 2-spin description

Figure 5 shows the 2-dimensional posterior densities for $\chi_{\rm eff} - \chi_p$[7] (left) and $\chi_{\rm eff} - q$ (right) obtained from both waveform models as well as the 1-dimensional prior distributions. Both plots demonstrate broad agreement with `IMRPhenomPv3` marginally favoring more unequal masses. This result is also consistent based on the comparisons to NR waveforms presented in the previous section. The posterior for χ_p is consistent with its prior, confirming the absence of evidence of spin-precession in GW151226. Overall we find that a re-analysis of the merger event GW151226 with our new waveform model does not provide new insights into the nature of the source but instead reinforces our current understanding of the source.

The consistency of the results implies that two-spin precession effects do not impact this signal in agreement with previous studies predicting that aligned-two-spin effects are not easily measurable [80]. However, it is possible that certain binaries and orientations might make it possible to measure both spins simultaneously. This could be achieved, for example, with precessing models that also include higher multipoles modes, or with louder signals observed by more detectors.

[7] Note that `IMRPhenomPv3` no longer explicitly uses the effective precession parameter χ_p. However we show it here for direct comparison to `IMRPhenomPv2` results.

Parameter	`IMRPhenomPv2`	`IMRPhenomPv3`
Primary Mass: $m_1(M_\odot)$	$13.68^{+7.93}_{-3.13}$	$14.45^{+10.23}_{-3.96}$
Secondar Mass: $m_2(M_\odot)$	$7.73^{+2.10}_{-2.41}$	$7.35^{+2.57}_{-2.52}$
Total Mass: $M_{\rm tot}(M_\odot)$	$23.37^{+6.00}_{-1.10}$	$23.80^{+8.33}_{-1.55}$
Mass ratio: q	$0.57^{+0.36}_{-0.32}$	$0.51^{+0.44}_{-0.31}$
Effective Spin: $\chi_{\rm eff}$	$0.19^{+0.18}_{-0.07}$	$0.20^{+0.23}_{-0.09}$
Precession Parameter: $\chi_{\rm p}$	$0.44^{+0.34}_{-0.28}$	$0.44^{+0.35}_{-0.28}$
Log Bayes Factor: Log($\mathcal{B}$)	50.707	51.291

TABLE II. Parameter Table for GW151226. Masses are defined in the source frame. We quote the median and the 90% symmetric credible interval of the 1D marginalised posterior distributions.

V. DISCUSSION

We have presented an upgrade to the phenomenological model `IMRPhenomPv2` called `IMRPhenomPv3`. This model predicts the GW polarisations computed using the the dominant $\ell = |m| = 2$ multipole in the co-precessing frame, from non-eccentric merging BBHs with generically orientated spins. Our upgrade consists of replacing the model for the precession dynamics of [23] that was derived under the assumption of a single spin precessing BBH system with the more accurate analytic model from [36, 37] that contains two-spin effects.

We have validated our new model against a large set of precessing NR waveforms. Although our selection of NR waveforms is biased towards mass-ratios < 3 and spin magnitudes < 0.5 we find that all three models consid-

ered generally perform well however, we have identified a clear region in parameter space, mass-ratios > 3 where all models begin to loose accuracy. Encouragingly we find that `IMRPhenomPv3` greatly outperforms the previous model for the most extreme case we considered, with the largest improvement being $\sim 12\%$. This improvement suggests that `IMRPhenomPv3` can be utilised in a much wider parameter space than `IMRPhenomPv2` was found to be reliable. We emphasise the importance of NR to continue to push the capabilities of precessing BBH simulations that will allow more stringent tests of waveforms models and ultimately lead to more accurate waveform models being developed.

As a first application we re-analysed GW151226 with our two-spin model and find consistent results compared with the single-spin model thereby reinforcing our current inference on the nature of GW151226.

As our waveform model is analytic one can evaluate the model using a non-uniform grid of frequencies. This is essential for methods such as ROQ [38] and the multi-banding technique of [81]. These methods can increase the computational efficiency of sampling-based parameter estimation by factors of 300 for low mass systems.

Finally we note that there are a number of physical effects that are ignored. We do not model any asymmetry between the positive and negative m modes which are responsible for large out-of-plane recoil kick velocities. In the underlying, aligned-spin model we do not include effects from higher order multipoles however, we have recently developed a method to do this [32] and we are currently determining the accuracy of a precessing model that includes higher order multipoles in the co-precessing frame.

ACKNOWLEDGMENTS

We thank Carl-Johan Haster for kindly supplying the PSD computed using `BayesWave` for the parameter estimation study of GW151226. We thank Sylvain Marsat for useful discussions. S.K. and F.O. acknowledge support by the Max Planck Society's Independent Research Group Grant. We thank the Atlas cluster computing team at AEI Hannover where this analysis was carried out. M.H. was supported by Science and Technology Facilities Coun- cil (STFC) grant ST/L000962/1 and European Research Council Consolidator Grant 647839. This work made use of numerous open source computational packages such as python [82], NumPy, SciPy [83], Matplotlib [84] and the GW data analysis software library `pycbc` [85].

[1] J. Aasi *et al.* (LIGO Scientific), Class. Quant. Grav. **32**, 074001 (2015), arXiv:1411.4547 [gr-qc].
[2] F. Acernese *et al.* (VIRGO), Class. Quant. Grav. **32**, 024001 (2015), arXiv:1408.3978 [gr-qc].
[3] B. P. Abbott *et al.* (LIGO and Virgo Scientific Collaboration), Phys. Rev. Lett. **116**, 061102 (2016), arXiv:1602.03837 [gr-qc].
[4] B. P. Abbott *et al.* (LIGO and Virgo Scientific Collaboration), Phys. Rev. Lett. **116**, 241103 (2016), arXiv:1606.04855 [gr-qc].
[5] B. P. Abbott *et al.* (LIGO and Virgo Scientific Collaboration), Phys. Rev. Lett. **118**, 221101 (2017), arXiv:1706.01812 [gr-qc].
[6] B. P. Abbott *et al.* (Virgo, LIGO Scientific), Phys. Rev. Lett. **119**, 141101 (2017), arXiv:1709.09660 [gr-qc].
[7] B. P. Abbott *et al.* (Virgo, LIGO Scientific), Astrophys. J. **851**, L35 (2017), arXiv:1711.05578 [astro-ph.HE].
[8] B. P. Abbott *et al.* (Virgo, LIGO Scientific), Phys. Rev. Lett. **119**, 161101 (2017), arXiv:1710.05832 [gr-qc].
[9] B. P. Abbott *et al.* (GROND, SALT Group, OzGrav, DFN, INTEGRAL, Virgo, Insight-Hxmt, MAXI Team, Fermi-LAT, J-GEM, RATIR, IceCube, CAASTRO, LWA, ePESSTO, GRAWITA, RIMAS, SKA South Africa/MeerKAT, H.E.S.S., 1M2H Team, IKI-GW Follow-up, Fermi GBM, Pi of Sky, DWF (Deeper Wider Faster Program), Dark Energy Survey, MASTER, AstroSat Cadmium Zinc Telluride Imager Team, Swift, Pierre Auger, ASKAP, VINROUGE, JAGWAR, Chandra Team at McGill University, TTU-NRAO, GROWTH, AGILE Team, MWA, ATCA, AST3, TOROS, Pan-STARRS, NuSTAR, ATLAS Telescopes, BOOTES, CalTechNRAO, LIGO Scientific, High Time Resolution Universe Survey, Nordic Optical Telescope, Las Cumbres Observatory Group, TZAC Consortium, LOFAR, IPN, DLT40, Texas Tech University, HAWC, ANTARES, KU, Dark Energy Camera GW-EM, CALET, Euro VLBI Team, ALMA), Astrophys. J. **848**, L12 (2017), arXiv:1710.05833 [astro-ph.HE].
[10] C. Messick, K. Blackburn, P. Brady, P. Brockill, K. Cannon, R. Cariou, S. Caudill, S. J. Chamberlin, J. D. E. Creighton, R. Everett, C. Hanna, D. Keppel, R. N. Lang, T. G. F. Li, D. Meacher, A. Nielsen, C. Pankow, S. Privitera, H. Qi, S. Sachdev, L. Sadeghian, L. Singer, E. G. Thomas, L. Wade, M. Wade, A. Weinstein, and K. Wiesner, Phys. Rev. D **95**, 042001 (2017).
[11] T. Dal Canton *et al.*, Phys. Rev. **D90**, 082004 (2014), arXiv:1405.6731 [gr-qc].
[12] S. A. Usman *et al.*, Class. Quant. Grav. **33**, 215004 (2016), arXiv:1508.02357 [gr-qc].
[13] A. H. Nitz, T. Dent, T. Dal Canton, S. Fairhurst, and D. A. Brown, Astrophys. J. **849**, 118 (2017), arXiv:1705.01513 [gr-qc].
[14] S. Klimenko, G. Vedovato, M. Drago, F. Salemi, V. Tiwari, G. A. Prodi, C. Lazzaro, K. Ackley, S. Tiwari, C. F. Da Silva, and G. Mitselmakher, Phys. Rev. D **93**, 042004 (2016).
[15] C. Cutler and E. E. Flanagan, Phys. Rev. **D49**, 2658 (1994), arXiv:gr-qc/9402014 [gr-qc].
[16] J. Veitch *et al.*, Phys. Rev. **D91**, 042003 (2015), arXiv:1409.7215 [gr-qc].
[17] B. P. Abbott *et al.* (Virgo, LIGO Scientific), Phys. Rev. Lett. **116**, 241102 (2016), arXiv:1602.03840 [gr-qc].

[18] T. A. Apostolatos, C. Cutler, G. J. Sussman, and K. S. Thorne, Phys. Rev. D **49**, 6274 (1994).
[19] L. E. Kidder, Phys. Rev. D **52**, 821 (1995).
[20] Y. Pan, A. Buonanno, A. Taracchini, L. E. Kidder, A. H. Mroué, H. P. Pfeiffer, M. A. Scheel, and B. Szilágyi, Phys. Rev. D **89**, 084006 (2014).
[21] A. Taracchini *et al.*, Phys. Rev. **D89**, 061502 (2014), arXiv:1311.2544 [gr-qc].
[22] S. Babak, A. Taracchini, and A. Buonanno, Phys. Rev. D **95**, 024010 (2017).
[23] M. Hannam, P. Schmidt, A. Bohé, L. Haegel, S. Husa, F. Ohme, G. Pratten, and M. Pürrer, Phys. Rev. Lett. **113**, 151101 (2014), arXiv:1308.3271 [gr-qc].
[24] L. Santamaría, F. Ohme, P. Ajith, B. Brügmann, N. Dorband, M. Hannam, S. Husa, P. Mösta, D. Pollney, C. Reisswig, E. L. Robinson, J. Seiler, and B. Krishnan, Phys. Rev. D **82**, 064016 (2010).
[25] S. Husa, S. Khan, M. Hannam, M. Pürrer, F. Ohme, X. J. Forteza, and A. Bohé, Phys. Rev. D **93**, 044006 (2016).
[26] S. Khan, S. Husa, M. Hannam, F. Ohme, M. Pürrer, X. Jiménez Forteza, and A. Bohé, Phys. Rev. **D93**, 044007 (2016), arXiv:1508.07253 [gr-qc].
[27] T. D. Abbott *et al.* (Virgo, LIGO Scientific), Phys. Rev. **X6**, 041014 (2016), arXiv:1606.01210 [gr-qc].
[28] B. P. Abbott *et al.* (Virgo, LIGO Scientific), Class. Quant. Grav. **34**, 104002 (2017), arXiv:1611.07531 [gr-qc].
[29] R. Sturani, S. Fischetti, L. Cadonati, G. M. Guidi, J. Healy, D. Shoemaker, and A. Viceré, Journal of Physics: Conference Series **243**, 012007 (2010).
[30] Y. Pan, A. Buonanno, M. Boyle, L. T. Buchman, L. E. Kidder, H. P. Pfeiffer, and M. A. Scheel, Phys. Rev. D **84**, 124052 (2011).
[31] A. K. Mehta, C. K. Mishra, V. Varma, and P. Ajith, Phys. Rev. **D96**, 124010 (2017), arXiv:1708.03501 [gr-qc].
[32] L. London, S. Khan, E. Fauchon-Jones, C. García, M. Hannam, S. Husa, X. Jiménez-Forteza, C. Kalaghatgi, F. Ohme, and F. Pannarale, Phys. Rev. Lett. **120**, 161102 (2018).
[33] R. Cotesta, A. Buonanno, A. Bohé, A. Taracchini, I. Hinder, and S. Ossokine, (2018), arXiv:1803.10701 [gr-qc].
[34] S. E. Field, C. R. Galley, J. S. Hesthaven, J. Kaye, and M. Tiglio, Phys. Rev. X **4**, 031006 (2014).
[35] J. Blackman, S. E. Field, M. A. Scheel, C. R. Galley, C. D. Ott, M. Boyle, L. E. Kidder, H. P. Pfeiffer, and B. Szilágyi, Phys. Rev. D **96**, 024058 (2017).
[36] K. Chatziioannou, A. Klein, N. Yunes, and N. Cornish, Phys. Rev. **D95**, 104004 (2017), arXiv:1703.03967 [gr-qc].
[37] K. Chatziioannou, A. Klein, N. Cornish, and N. Yunes, Phys. Rev. Lett. **118**, 051101 (2017), arXiv:1606.03117 [gr-qc].
[38] R. Smith, S. E. Field, K. Blackburn, C.-J. Haster, M. Pürrer, V. Raymond, and P. Schmidt, Phys. Rev. **D94**, 044031 (2016), arXiv:1604.08253 [gr-qc].
[39] P. Schmidt, M. Hannam, S. Husa, and P. Ajith, Phys. Rev. D **84**, 024046 (2011).
[40] R. O'Shaughnessy, B. Vaishnav, J. Healy, Z. Meeks, and D. Shoemaker, Phys. Rev. D **84**, 124002 (2011).
[41] L. Pekowsky, R. O'Shaughnessy, J. Healy, and D. Shoemaker, Phys. Rev. D **88**, 024040 (2013).
[42] A. Buonanno, Y.-b. Chen, and M. Vallisneri, Phys. Rev. **D67**, 104025 (2003), [Erratum: Phys. Rev.D74,029904(2006)], arXiv:gr-qc/0211087 [gr-qc].
[43] P. Schmidt, M. Hannam, and S. Husa, Phys. Rev. D **86**, 104063 (2012).
[44] M. Boyle, R. Owen, and H. P. Pfeiffer, Phys. Rev. D **84**, 124011 (2011).
[45] P. Schmidt, F. Ohme, and M. Hannam, Phys. Rev. D **91**, 024043 (2015).
[46] S. Droz, D. J. Knapp, E. Poisson, and B. J. Owen, Phys. Rev. **D59**, 124016 (1999), arXiv:gr-qc/9901076 [gr-qc].
[47] `https://dcc.ligo.org/LIGO-T1500602`.
[48] X. Jiménez-Forteza, D. Keitel, S. Husa, M. Hannam, S. Khan, and M. Pürrer, Phys. Rev. D **95**, 064024 (2017).
[49] B. P. Abbott *et al.* (LIGO Scientific Collaboration and Virgo Collaboration), Phys. Rev. Lett. **116**, 131103 (2016).
[50] B. P. Abbott *et al.* (LIGO Scientific Collaboration and Virgo Collaboration), Phys. Rev. Lett. **116**, 241102 (2016).
[51] B. P. Abbott *et al.* (LIGO Scientific and Virgo Collaborations), Phys. Rev. Lett. **116**, 221101 (2016).
[52] B. P. Abbott *et al.* (LIGO Scientific Collaboration and Virgo Collaboration), Phys. Rev. X **6**, 041015 (2016).
[53] S. Vitale, D. Gerosa, C.-J. Haster, K. Chatziioannou, and A. Zimmerman, Phys. Rev. Lett. **119**, 251103 (2017), arXiv:1707.04637 [gr-qc].
[54] T. Dietrich *et al.*, (2018), arXiv:1804.02235 [gr-qc].
[55] B. P. Abbott *et al.* (Virgo, LIGO Scientific), (2018), arXiv:1805.11579 [gr-qc].
[56] B. P. Abbott *et al.* (Virgo, LIGO Scientific), (2018), arXiv:1805.11581 [gr-qc].
[57] P. Schmidt, "Studying and modelling the complete gravitational-wave signal from precessing black hole binaries," `https://orca.cf.ac.uk/64062/`.
[58] M. Kesden, D. Gerosa, R. O'Shaughnessy, E. Berti, and U. Sperhake, Phys. Rev. Lett. **114**, 081103 (2015).
[59] A. Klein, N. Cornish, and N. Yunes, Phys. Rev. **D88**, 124015 (2013), arXiv:1305.1932 [gr-qc].
[60] K. Chatziioannou, A. Klein, N. Yunes, and N. Cornish, Phys. Rev. **D88**, 063011 (2013), arXiv:1307.4418 [gr-qc].
[61] C. M. Bender and S. A. Orszag, *Advanced mathematical methods for scientists and engineers 1, Asymptotic methods and perturbation theory* (Springer, New York, 1999).
[62] A. Klein, N. Cornish, and N. Yunes, Phys. Rev. D **90**, 124029 (2014).
[63] M. Cabero, A. B. Nielsen, A. P. Lundgren, and C. D. Capano, Phys. Rev. D **95**, 064016 (2017).
[64] B. Bruegmann, J. A. Gonzalez, M. Hannam, S. Husa, and U. Sperhake, Phys. Rev. **D77**, 124047 (2008), arXiv:0707.0135 [gr-qc].
[65] I. Harry, S. Privitera, A. Bohé, and A. Buonanno, Phys. Rev. D **94**, 024012 (2016).
[66] I. Harry, J. Calderón Bustillo, and A. Nitz, Phys. Rev. **D97**, 023004 (2018), arXiv:1709.09181 [gr-qc].
[67] `https://wiki.ligo.org/DASWG/LALSuite`.
[68] P. Schmidt, I. W. Harry, and H. P. Pfeiffer, (2017), arXiv:1703.01076 [gr-qc].
[69] E. Hamilton and M. Hannam, arXiv, 1807.06331 (2018), arXiv:1807.06331 [gr-qc].
[70] `https://dcc.ligo.org/LIGO-T0900288/public`.
[71] A. H. Mroué, M. A. Scheel, B. Szilágyi, H. P. Pfeiffer, M. Boyle, D. A. Hemberger, L. E. Kidder, G. Lovelace, S. Ossokine, N. W. Taylor, A. i. e. i. f. Zenginoğlu, L. T. Buchman, T. Chu, E. Foley, M. Giesler, R. Owen, and

S. A. Teukolsky, Phys. Rev. Lett. **111**, 241104 (2013).
[72] https://data.black-holes.org/waveforms/index.html.
[73] J. Healy, C. O. Lousto, Y. Zlochower, and M. Campanelli, Classical and Quantum Gravity **34**, 224001 (2017).
[74] http://ccrg.rit.edu/~RITCatalog/.
[75] K. Jani, J. Healy, J. A. Clark, L. London, P. Laguna, and D. Shoemaker, Classical and Quantum Gravity **33**, 204001 (2016).
[76] http://www.einstein.gatech.edu/catalog/.
[77] J. Veitch, V. Raymond, B. Farr, W. Farr, P. Graff, S. Vitale, *et al.*, Phys. Rev. D **91**, 042003 (2015), arXiv:1409.7215 [gr-qc].
[78] T. B. Littenberg and N. J. Cornish, Phys. Rev. **D91**, 084034 (2015), arXiv:1410.3852 [gr-qc].
[79] N. J. Cornish and T. B. Littenberg, Class. Quant. Grav. **32**, 135012 (2015), arXiv:1410.3835 [gr-qc].
[80] M. Pürrer, M. Hannam, and F. Ohme, Phys. Rev. **D93**, 084042 (2016), arXiv:1512.04955 [gr-qc].
[81] S. Vinciguerra, J. Veitch, and I. Mandel, Class. Quant. Grav. **34**, 115006 (2017), arXiv:1703.02062 [gr-qc].
[82] https://www.python.org/.
[83] E. Jones, T. Oliphant, P. Peterson, *et al.*, "SciPy: Open source scientific tools for Python," (2001–).
[84] J. D. Hunter, Computing In Science & Engineering **9**, 90 (2007).
[85] A. Nitz *et al.*, "pycbc software," (2018).